Mapping the Pore Architecture of Structured Catalyst Monoliths from nm to cm Scale with Electron and X-ray Tomography

Johannes Becher[1], Thomas L. Sheppard[1,2,*], Yakub Fam[1], Sina Baier[3], Wu Wang[4], Di Wang[4], Satishkumar Kulkarni[5], Thomas F. Keller[5,6], Mikhail Lyubomirskiy[5], Dennis Brueckner[5,6,7], Maik Kahnt[5,6], Andreas Schropp[5], Christian G. Schroer[5,6], and Jan-Dierk Grunwaldt[1,2,*]

[1]Institute for Chemical Technology and Polymer Chemistry, Karlsruhe Institute of Technology (KIT), Engesserstr. 20, 76131 Karlsruhe, Germany

[2]Institute of Catalysis Research and Technology, Karlsruhe Institute of Technology (KIT), Hermann-von-Helmholtz Platz 1, 76344 Eggenstein-Leopoldshafen, Germany

[3]Department of Physics, Technical University of Denmark (DTU), Fysikvej 311, 2800 Kgs. Lyngby, Denmark

[4]Institute of Nanotechnology, Karlsruhe Institute of Technology, Hermann-von-Helmholtz Platz 1, 76344 Eggenstein-Leopoldshafen, Germany

[5]Deutsches Elektronen-Synchrotron DESY, Notkestraße 85, 22607 Hamburg, Germany

[6]Department Physik, Universität Hamburg, Luruper Chaussee 149, 22761 Hamburg, Germany

[7]Faculty of Chemistry and Biochemistry, Ruhr-University Bochum, Universitätsstr. 150, 44801 Bochum, Germany

Corresponding authors: thomas.sheppard@kit.edu; grunwaldt@kit.edu

Abstract

The hierarchical pore systems of Pt/Al$_2$O$_3$ exhaust gas aftertreatment catalysts were analyzed with a collection of correlative imaging techniques to monitor changes induced by hydrothermal aging. Synergistic imaging with laboratory X-ray microtomography, synchrotron radiation ptychographic X-ray computed nanotomography and electron tomography allowed quantitative observation of the catalyst pore architecture from cm to nm scale. Thermal aging at 750 °C in air and hydrothermal aging at 1050 °C in 10% H$_2$O/air caused increasing structural degradation, which manifested as widespread sintering of Pt particles, increased volume and quantity of macropores (>20 nm), and reduction in effective surface area coupled to decreasing volume and frequency of mesopores (2-20 nm) and micropores (<2 nm). Electron tomography unraveled the 3D structure with high resolution allowing visualization of meso- and macropores, but with samples of maximum 300 nm thickness. To complement this, hard X-ray ptychographic tomography produced quantitative 3D electron density maps of 5 µm diameter samples with spatial resolution <50 nm, effectively filling the resolution gap between electron tomography and hard X-ray microtomography. The obtained 3D volumes are an essential input for future computational modelling of fluid dynamics, mass transport or diffusion properties and may readily complement bulk 1D porosimetry measurements or simulated porosity.

Introduction

The removal of pollutants such as CO, NO$_x$ and hydrocarbons plays a pivotal role in exhaust gas aftertreatment of combustion engines, which is enforced through increasingly strict emissions control legislation in Europe and worldwide [1-4]. Most prominently used for this process are supported noble metal catalysts such as Pt, Pd or Rh, which are expensive and in limited supply [1, 5]. Even incremental improvements in catalyst efficiency and long-term activity can therefore strongly impact production costs, sustainability and environmental benefits of the catalyst [3]. In industrial and automotive (i.e 'real

world') applications, catalysts are typically prepared as thin washcoat layers on porous ceramic monoliths. This maximizes the surface area and improves gas flow properties to the active metal sites, mainly located within the catalyst washcoat pores [6-7]. In contrast, catalytic activity measurements, spectroscopic or diffraction studies on laboratory scale are commonly performed with model powder catalysts (e.g. Pt/Al_2O_3) or pellets in fixed bed reactors or in situ sample environments [8]. For example, analysis of gas adsorption with infrared (IR) spectroscopy, particle size with X-ray diffraction (XRD), or metal oxidation state with X-ray absorption spectroscopy (XAS) [9-11]. In most cases knowledge transfer to real world applications is limited, since the native catalyst form is a washcoated monolith and not a sieved powder or compressed pellet. Fundamental knowledge of the pore system in hierarchically-structured catalysts is also important to understand reactant diffusion, accessibility of active sites and structural integrity [12-14]. Porosity is often examined using methods such as Hg porosimetry or gas adsorption isotherms, which can be regarded as one-dimensional bulk analyses. However, exhaust gas catalysts have a complex hierarchical composition, including porous ceramic monolith, washcoated catalyst layers, multiscale porosity within the layers, and active metal nanoparticles, therefore such bulk characterization is not optimal to probe the structure and function of the catalyst. Modeling and simulation are also frequently used to predict or define relationships between pore architecture and catalytic performance [15-17]. Such simulations would benefit greatly from accurate understanding of the real pore structures of the catalyst washcoat. Thus a spatially-resolved analytical approach considering: (i) micro-, meso- and macropores across length scales from nm to cm, and (ii) distribution of catalytic active sites within the pores, is necessary from the perspective of both microkinetics (e.g. metal particle size, dispersion) and macrokinetics (e.g. transport porosity, fluid dynamics) [18-21]. As a typical exhaust gas catalyst experiences long-term use under dynamic operating conditions, the stability of the pore system and active metal sites is crucial [3, 22], particularly the effects of (hydro)thermal aging on pore size and distribution [23].

Addressing this need for spatially-resolved characterization, tomography with hard X-rays and electrons constitute powerful techniques for analysis of sample interiors in a structurally non-invasive manner [19, 23-26]. Tomography allows volumetric 3D imaging of the material structure which can be directly applied to modelling studies. This is advantageous compared to the approximations necessary when using conventional bulk one-dimensional porosity metrics to estimate 3D porosity [27-29]. Electron tomography (ET) is an extension of transmission electron microscopy (TEM) and is an established characterization tool which routinely offers spatial resolution down to about 1 nanometer, allowing visualization of micro- and mesopore networks [18, 30]. Complementary energy-dispersive X-ray spectroscopy (EDX) can also determine the location, size and distribution of metal nanoparticles in porous materials. The key disadvantage of ET is the relatively low penetration of electrons through the material, which typically limits the potential field of view (FOV) and sample thickness to several hundred nm. This is not optimal for catalyst materials where structure and function are closely linked, and heterogeneous nature means that small sample volumes may not be representative of the bulk material [31-33]. In contrast, modern synchrotron radiation sources enable hard X-ray tomography on much larger samples, offering high photon flux, tunable energy, and a variety of contrast methods [24-25]. One emerging technique known as ptychographic X-ray computed tomography (PXCT) is particularly promising for catalysis and materials research [34-36]. Ptychography (scanning coherent diffraction imaging) exceeds the resolution limitations of conventional lens-based methods and offers spatial resolution not limited by the probe beam size. Ptychographic image reconstruction can retrieve both attenuation and phase shift of the transmitted X-ray beam, allowing calculation of local electron density of the sample and therefore quantitative identification of individual features [37]. Although ET offers superior spatial resolution than any X-ray method, PXCT can image sample volumes on the order of μm, and has proven resolution down to 35 nm for catalyst particles [38], and 16 nm for model nanoporous materials [39-42]. PXCT therefore offers an optimal route for characterization of meso- and macropores on extended sample volumes, and

combined with ET provides new opportunities for structural and chemical characterization of catalysts and porous materials [38, 43].

In this work we have characterized Pt-based catalyst monoliths for exhaust gas aftertreatment with complementary multiscale tomography methods, including: (i) laboratory X-ray microtomography (μ-CT), (ii) ET and (iii) synchrotron-based hard X-ray PXCT. Firstly, cordierite monoliths were washcoated with Pt/Al_2O_3 and characterized for CO oxidation activity. Different thermal and hydrothermal treatment protocols were then used to simulate the effects of long-term catalyst aging experienced in automotive emissions control systems. The hierarchical catalyst structure including the active metal species and interior pore systems were then visualized over length scales from nm to cm with tomography. Non-invasive characterization of catalyst structures is demonstrated as essential to accurately define delicate interior features and pore network topologies, which can aid in understanding aging processes in catalyst monoliths across all relevant length scales.

Experimental Section

Sample Preparation

4 wt.% Pt on Al_2O_3 was prepared by incipient wetness impregnation of γ-Al_2O_3 with an aqueous solution of tetraammineplatinum(II) nitrate (Sigma-Aldrich) to obtain 4 wt.% Pt loading with respect to the used γ-Al_2O_3 support. The powder was dried for 12 hours at 80 °C and then calcined at 500 °C for 2 hours in a static air furnace. From a larger cordierite monolith with 400 channels per square inch (cpsi), cylindrical samples of about 19 mm diameter and 20 mm height were drilled out. An aqueous suspension of the catalyst powder containing 10 wt.% commercial colloidal silica binder (Ludox AS-40) was prepared. To obtain a Pt load of 3.53 mg cm^{-3}, this slurry was applied to the honeycomb body under gravity using a pipette, allowing the slurry to progress along the monolith channels. After excess suspension had dripped off, the monolith was dried and weighed to approximate the washcoat loading by mass. This

procedure was repeated until 0.6 g of the washcoat had deposited and the desired loading had been achieved. The honeycombs were then dried overnight at 80 °C and calcined in static air at 500 °C for 2 hours. The resulting honeycombs were regarded as typical model exhaust gas monolith catalysts.

Sample Conditioning by (Hydro-) thermal Aging

In order to simulate structural changes and degradation of the catalyst pore system during its operational lifetime, the monolith samples were conditioned to mimic various degrees of catalyst aging according to the conditions shown in Table 1. One of the three honeycombs was used as prepared without any aging procedure, the second was thermally aged and the third was hydrothermally aged. The samples are referred to as 'fresh', 'aged' and 'severely aged', respectively. To avoid potential damage resulting from rapid temperature changes, heating or cooling ramps of maximum 20 K min^{-1} were applied during conditioning.

Table 1. Overview of artificial aging conditions for the Pt/Al$_2$O$_3$ monoliths

Sample	Treatment
Monolith 1 – Fresh	Used as prepared
Monolith 2 – Aged	4h, 750 °C, static air furnace
Monolith 3 – Severely Aged	12h, 1050 °C, 10% H$_2$O, 2 Lmin^{-1}, plug-flow reactor

Catalyst Characterization

The surface area and mean pore diameter of the calcined 4 wt.% Pt/Al$_2$O$_3$ powder prior to washcoating, and the washcoat of the fresh, aged and severely aged samples following (hydro)thermal treatment, was determined by N$_2$-physisorption followed by BET and BJH analysis as described in previous work [44]. Catalytic performance was tested with CO oxidation light off measurements (1000 ppm CO, 10 vol.% O$_2$ in nitrogen) with a heating ramp of 3 K/min up to 250 °C. The washcoated honeycombs (19*20 mm, diameter*height) were placed in a glass tube reactor of 2.5 cm diameter and the position fixed with glass wool. A gas hourly space velocity (GHSV) of 50000 h^{-1} resulting in a flow of 4725 ml/min

was used. Further details on catalytic tests can be found in the supporting information (Table S1, Figure S3-5).

TEM was used to analyze the Pt particle size and dispersion along with the nanoscale composition of the catalysts. Catalyst specimens from each of the three washcoated monoliths (fresh, aged and severely aged) were removed by physical abrasion and dry dispersed on holey carbon coated copper TEM grids. Samples were examined in a FEI Titan 80-300 aberration-corrected electron microscope (FEI, USA) operated at 300 kV in STEM mode with a high-angle annular dark-field (HAADF) detector, at Karlsruhe Nano Micro Facility (KNMF) of Karlsruhe Institute of Technology (Karlsruhe, Germany). To characterize the Pt particle size distribution, the Pt particles were marked and counted manually across several STEM images (see supporting information Figure S2).

X-ray Micro Computed Tomography

Laboratory μ-CT experiments were performed with an Xradia 410 Versa (Carl Zeiss AG, Germany) tomography setup at the 3D Imaging Center at the Technical University of Denmark (DTU, Kgs. Lyngby, Denmark) with the fresh, aged and severely aged monoliths. Firstly, the complete honeycombs (19 mm diameter, 20 mm height) were measured (40 kV, 10 W, filter: LE 2, exposure: 2 s, binning: 2*2, 1601 projections, reconstructed pixel size: 27 μm) as obtained after the aging steps (Table 1) to provide a structural overview (Figure 1a). Afterwards, single channels of the fresh, aged and severely aged samples were cut out from the honeycomb structure with a razor and analyzed (40 kV, 10 W, 10X objective, filter: none, binning 2*2, 3201 projections, 60 s exposure per projection, reconstructed pixel size: 0.7 μm) to examine more closely the washcoat and cordierite structure (Figure 1b). Image reconstruction was performed using the inbuilt acquisition and reconstruction software Scout-and-ScanTM Control System Reconstructor 11.8043.19515 (Carl Zeiss AG, Germany) which is based on a Feldkamp, Davis and Kress algorithm using filtered back-projection [45] Spatial resolution was estimated to be approximately 3 times the reconstructed pixel size.
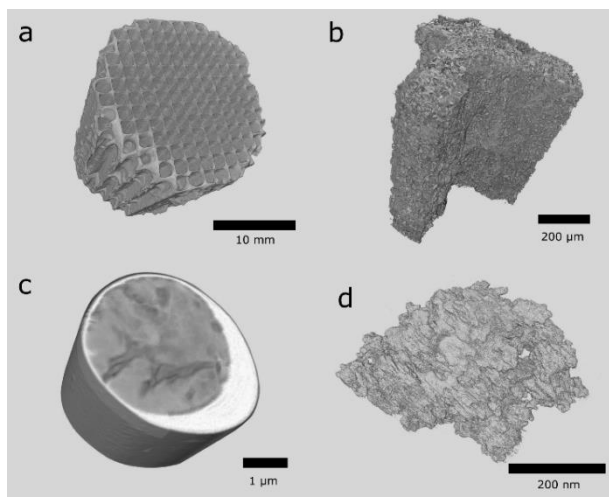
Figure 1. Overview of multiscale tomography measurements of 4 wt. % Pt/Al_2O_3 washcoated emission control monoliths: (a) complete monolith analyzed by μ-CT at ca. 80 μm and (b) ca. 2 μm 3D spatial resolution; (c) washcoat section analyzed by PXCT (<50 nm resolution); (d) washcoat particle analyzed by TEM-tomography (<5 nm resolution).

Ptychographic X-ray Computed Tomography

Conical sections of the 4% Pt/Al_2O_3 catalyst washcoat were extracted via Ga^+ focused ion beam (FIB) milling and transferred to a custom-made titanium tomography pin sample holder at DESY NanoLab [46]. The resulting sample dimensions were approximately 20 to 30 μm in height, with diameter of 3 μm (top) to 8 μm (bottom) (see supporting information Figure S6-7).

PXCT measurements in combination with X-ray fluorescence (XRF) and XRD (see supporting information Figure S8-9) were performed at the hard X-ray nanoprobe endstation of beamline P06 at the PETRA III synchrotron radiation source (Hamburg, Germany). The sample holder pins were mounted on the ptychographic nano-analytical microscope (PtyNAMi) setup, equipped with an interferometric positioning system to track the sample position relative to the optics. All measurements were performed at ambient temperature and in air. The X-ray photons with an energy of 15 keV were focused to a spot size of 124 x 124 nm with nano focusing lenses (NFL), providing a coherent flux of about $2.5*10^7$

8

photons/s on the sample. An Eiger X 4M detector (Dectris, Switzerland) was placed 4160 mm

downstream of the sample. For collection of tomography data, 2D projections of the sample were

recorded over a rotational range of 180° in 1° steps and afterwards reconstructed into 3D volumes (see

below). Total acquisition time for each PXCT tomogram was approximately 35 h. For the combination of

ptychography, XRF and XRD measurements, the sample was placed in the focal spot of the beam.

Measurement parameters for each sample are shown in Table 2.

Table 2. Experimental parameters for the PXCT measurements at P06 beamline of PETRA III

Sample	FOV[a] [μm²]	Sample diameter [μm]	Step size[a] [nm]	Exposure time [ms]	Scan time per projection [min]
Fresh	3.5*5.2	4.5	25*25	20	12.5
Aged	5.0*6.7	5.0	40*40	20	9.3
Severely aged	3.5*5.1	4.0	25*25	20	11.75

[a] vertical x horizontal

Electron Tomography

For ET studies, the washcoat powder was removed from the monoliths by physical abrasion. ET

measurements were performed using a tomography holder (E.A. Fischione Instruments, USA) positioned

within a Titan 80-300 aberration-corrected electron microscope (FEI, USA) operated at an accelerating

voltage of 300 kV in STEM mode. Access to ET was provided by Karlsruhe Nano Micro Facility (KNMF) at

Karlsruhe Institute of Technology (Karlsruhe, Germany). The tilt series of high-angle annular dark-field

(HAADF) STEM images were collected with the Xplore3D software (FEI, USA) over a tilt range of ±60°,

with tilt increment of 2°. Alignment of the tilt series was performed in IMOD software using the cross-

correlation function. The aligned tilt series were reconstructed using the simultaneous iterative

reconstruction technique (SIRT) with 25 iterations in the Inspect3D software (FEI, USA) and the resultant

reconstructed tomograms had a final voxel size of 0.46 or 0.64 nm depending on the magnification.

Spatial resolution was estimated by sharp edge fitting of a typical sharp feature in the final reconstructed volume (see supporting information Figure S22).

Data and Image Processing

The diffraction patterns recorded during the PXCT experiment were cropped to 512*512 detector pixels, leading to a pixel size of 8.95 nm in the reconstructed ptychography projections. The reconstructions of the projection images were performed on Nvidia Tesla P100 graphics processing units (GPU) using the ePIE algorithm [47]. Reconstruction artefacts such as phase wedges were removed from the projections. Subsequently the projection images were aligned to each other using a correlation of horizontal line integrals for relative vertical positioning, and the center of mass of vertical line integrals for relative horizontal positioning [48]. Finally, tomographic reconstruction was performed using the gridrec-algorithm implemented in the tomopy package to generate 3D volumes [49-50]. The resulting phase and amplitude volumes were offset corrected, by setting the air around the sample to have zero phase shift and zero absorption. To calculate the effective 3D electron density distribution, the values of the phase volumes were divided by the incident beam wavelength, the classical electron radius and the edge length of the reconstructed cubic voxels as described in the literature [37]. Reference electron density values for Pt, Al_2O_3 and Ga were calculated from common tabulated mass density values (Al_2O_3: 3.95 g cm^{-3}, Pt: 21.45 g cm^{-3}, Ga: 5.9 g cm^{-3}).

During the beamtime, the achievable spatial resolution of the ptychography reconstructions was estimated using Fourier ring correlation (FRC) of two reconstructed opposing projections (e.g. -90° and 90°) from each dataset [51]. After the beamtime, the complete 3D datasets were halved and used to reconstruct two volumes each. The Fourier shell correlations (FSC) of these pairs of volumes all resulted in lower values than the Crowther limit, therefore they represent only the similarity of the volumes to this feature size but not the actual given resolution, which was assumed to be the Crowther limit [52] for each dataset: 35.3 nm , 47.8 nm and 41.0 nm for the fresh, aged and severely aged volumes respectively.

10

The 3D volumes obtained by µ-CT, PXCT and ET were visualized, filtered and segmented using Avizo 9.3 software (ThermoFisher Scientific, USA), in order to visualize the different sample components. A more detailed description of the data processing steps can be found in the supporting information. For better comparability the same data treatment protocol for PXCT and ET was employed.

Results

Catalyst Characterization

The average pore size and surface area of the bulk washcoat was determined by BET measurements of the freshly prepared 4 wt.-% Pt/Al_2O_3 catalyst powder, which showed an initial BET surface area of 160 m²/g and calculated mean pore diameter of 11.8 nm. In addition, the monolith washcoats were analyzed via BET and BJH measurements, following careful removal of about 150 mg of washcoat from each monolith. The results are shown in Table 3 (for plots see Figure S1). The BET results show an isotherm type II behavior and sequential decrease in surface area from the fresh, to the aged and severely aged samples, with a corresponding increase of the mean pore size observed by BJH analysis. The BJH plot of the fresh sample shows two peak maxima at approximately 4.5 and 6 nm. In the aged sample only the 6 nm peak was observed, while the severely aged sample showed no defined peak maxima below 10 nm. The combination of lower surface area and larger average pore diameter indicates a sequential transition from micropores and smaller mesopores, towards larger mesopores in the bulk material as a result of (hydro)thermal aging. Note that these are 1-dimensional average measurements of the total porosity in the sample.

Table 3. Results from the BET and BJH measurements of the fresh, aged and severely aged sample

Sample	BET area [m²/g]	BJH pore diameter [nm]
Fresh	90	4.6
Aged	66	6.1

Severely Aged	31	10.8

Following preparation of Pt/Al$_2$O$_3$ washcoats on three identical cordierite monoliths, each monolith was initially tested for CO oxidation activity before (hydro)thermal aging to ensure equivalent catalytic properties and account for any variation as a result of catalyst preparation [53]. Two of the monoliths were then thermally aged, and one of the two subsequently treated by hydrothermal aging, with the CO activity tests repeated after each treatment step. The average measured temperatures for 20% (T$_{20}$), 50% (T$_{50}$, defined as the light off temperature) and 80% (T$_{80}$) CO conversion for each monolith are shown in Figure 2. The individual results of each experiment are shown and tabulated in the supporting information (Table S1, Figure S3-5). In all cases two reaction cycles were performed and the conversion measured over the second cycle, to allow for degreening of the monolith performance [53]. The thermal and hydrothermal treatment procedures had a clear detrimental effect on catalyst performance, with the light off temperature increasing from 133, to 167, and to 183 °C for the fresh, aged and severely aged catalysts respectively. The same trend was also shown in the T$_{20}$ and T$_{80}$ temperatures. The results indicate the success of the aging treatment at inducing the desired detrimental structural and therefore activity changes in the catalyst [22, 54], which are commonly understood to result from sintering and change in pore diameters in the literature.
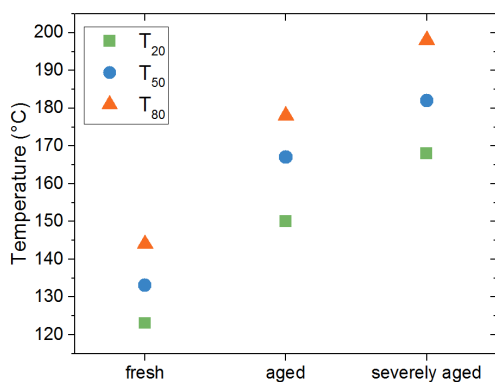
Figure 2. T_{20}, T_{50} and T_{80} temperature points observed during CO oxidation on the Pt/Al$_2$O$_3$ monoliths at each aging step. Fresh = average of 3 experiments, aged = average of 2 experiments.

The Pt particle size distribution in the washcoat of the three samples shown in Figure 3 was measured by particle counting from STEM images. A noticeable sintering of platinum occurred during aging, thus leading to an increase of the average Pt particle size from 1.6 nm to 3.8 nm to 41.0 nm for the fresh, very aged and severely aged catalysts (Figure 4) [22, 54]. This is furthermore reflected in the decreased total number of particles counted with increased aging. In addition to Pt sintering, for the severely aged sample a noticeable increase in apparent particle size and crystallinity was observed for the Al$_2$O$_3$ support, indicating significant changes in the pore structure and surface area. This was further confirmed by the presence of distinct Al$_2$O$_3$ reflexes observed by XRD following hydrothermal treatment, and the absence of these features in the fresh and aged monolith samples. XRD data was recorded simultaneously during PXCT studies (see supporting information Figure S9). In summary, catalyst characterization by TEM and activity testing revealed typical deactivation behavior, resulting from sintering of Pt particles and therefore an expected reduction in total surface area. However, a deeper analysis of the monolith and washcoat structure by spatially-resolved methods was necessary to more closely quantify the potential effects of changing pore structure as a concurrent deactivation pathway.
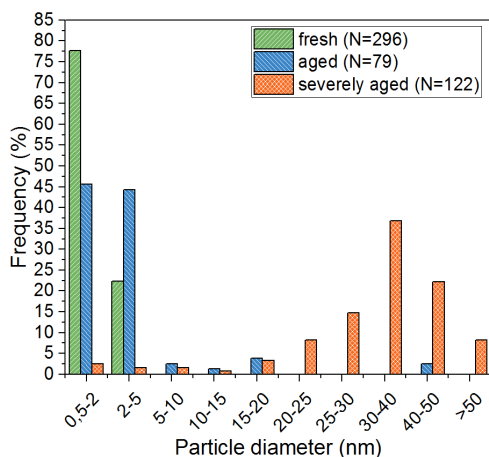
Figure 3. Histogram of Pt particle size distribution obtained from STEM analysis of Pt/Al$_2$O$_3$ washcoat material after different stages of (hydro)thermal aging; N = number of counted particles.
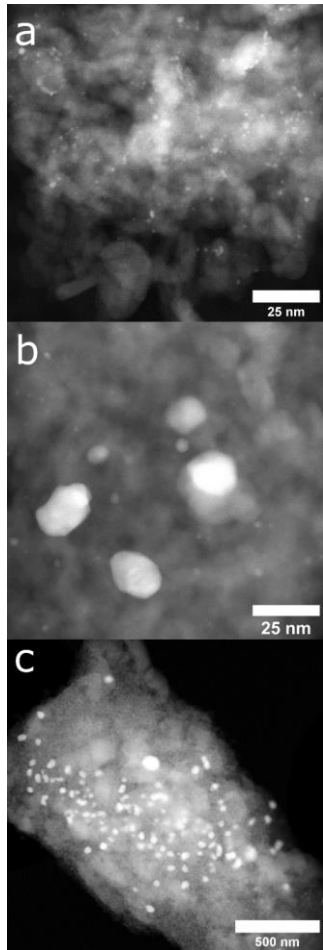

Figure 4. HAADF-STEM images of: (a) fresh, (b) aged and (c) severely aged Pt/Al$_2$O$_3$ washcoat material.

X-ray Micro Computed Tomography

To compare with initial characterization by BET, TEM and catalytic activity tests, the washcoat structure of the complete monoliths and single channels of each sample were examined by laboratory μ-CT. All measurements were performed after the monoliths had been used for catalytic tests. An example of the complete fresh monolith and a cut-out of a single corner of one channel are shown in Figure 5 (for further images see supporting information S10-14). The volumes had an estimated spatial resolution of 80 and 2 μm, respectively. The results show relatively uniform washcoat distribution between different

channels (Figure S11), which allowed selection and physical removal of appropriate sampling regions for the higher resolution scans.
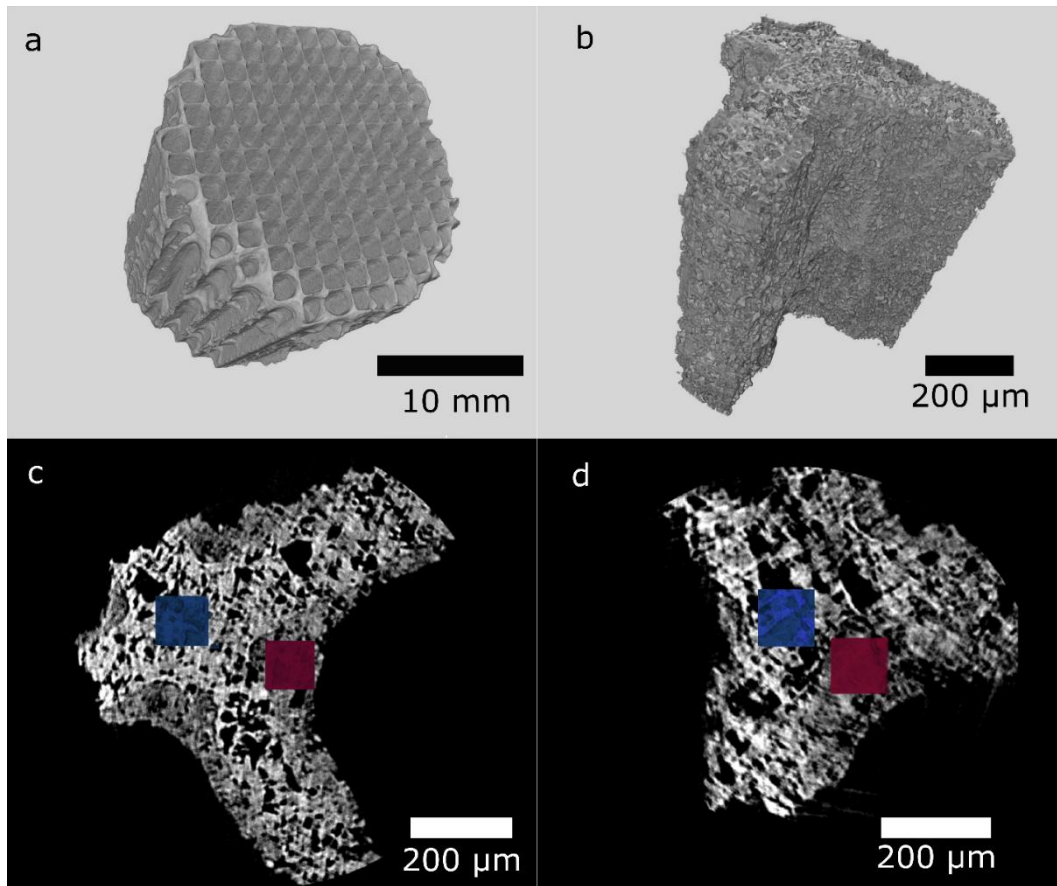

Figure 5. Volumetric representations of the reconstructed volumes of the fresh monolith obtained by μ-CT: (a) full monolith with ca. 80 μm resolution; (b) cut-out from a single corner of one channel with ca. 2 μm resolution; Orthographic slice of the fresh (c) and severely aged (d) cut-out from a single corner of one channel with ca. 2 μm resolution with marked sub-volumes from the cordierite structure (blue) and washcoat (red)

While laboratory X-ray sources allow continuous access to tomography, these operate with lower flux and typically lower spatial resolution compared to X-rays generated at synchrotron light sources. In this case due to the wide range of incident X-rays up to 40 kV (white beam), a definitive separation between the cordierite support and the catalyst washcoat based on absorption contrast was not clearly observed

and was difficult to visualize in a volumetric representation. Since a distinction and threshold segmentation between washcoat and cordierite could not be made directly with the image histogram due to a lack of contrast (see Figure S13), several sub-volumes were selected manually (Figure Figure **5**c-d). The cordierite monolith is known to have a geometric cross shape, which is partially visible as the lighter gray area in the center of Figure 5b-c. The darker appearance of the cross exterior indicates the presence of denser and more absorbing 4 wt.% Pt/Al_2O_3 washcoat, in contrast to the cordierite which was absent of Pt. On the high-resolution scans of single channels from the fresh and severely aged monoliths, the pore size distribution and relative change due to hydrothermal aging were analyzed by selecting specific sub-volumes of the washcoat, and segmenting the interior pore volume of these sub-volumes. Unless otherwise stated, the following discussion refers only to the washcoat material as the active catalyst, rather than the cordierite support. The obtained results are shown in Figure 6, with the segmentation process illustrated in the supporting information (Figure S14). Over 80 % of pores labelled within the fresh monolith cut-out were within the 5 to 10 µm diameter bracket, while the severely aged monolith showed a much broader visible pore size distribution, with a relatively high frequency of pores between 30 to 45 µm diameter. The minimum permitted pore diameter during counting was set to 5 µm to reflect the spatial resolution of the measurement, although counting parameters can be easily adapted. Notably, the total number of pores counted for the severely aged monolith (1103) was less than half that of the fresh monolith (2600). Furthermore, several cracks were seen to evolve in the washcoat layer (see supporting information Figure S12) [55]. The results indicate a significant increase in macroporosity as a result of hydrothermal aging, which may include the combination of individual smaller pores or channels into larger connected structures. This is expected to contribute to decreased surface area and also promote sintering of Pt species hosted within the pores [56]. The total porosity was quantified by selecting and averaging several sub-volumes from areas judged to consist mainly of washcoat material as described above (e.g. from the corner of the channel), resulting in a total porosity

measurement of 19.4 % for the fresh sample, slightly increasing to 21.1 % for the severely aged sample, although this probably lies within experimental error and is not significant. It should be reinforced that this analysis only relates to very large macropores above the chosen measuring limit of 5 μm, which reflects the spatial resolution limitation involved in μ-CT.

It is important to note that some studies suggest mild hydrothermal aging can have negligible effects on catalytic activity for CO oxidation [55], or even beneficial effects for oxidation of larger species (e.g. xylene) due to the increase in pore diameter [56]. Here hydrothermal aging was performed for 12 hours at 1050 °C. This was intended to simulate catastrophic aging of the catalyst washcoat structure and a high level of sintering, allowing more distinctive comparison with the fresh and thermally aged samples. It is therefore very important to carefully distinguish the aging conditions applied and the target reaction being investigated when considering other results in literature [22].
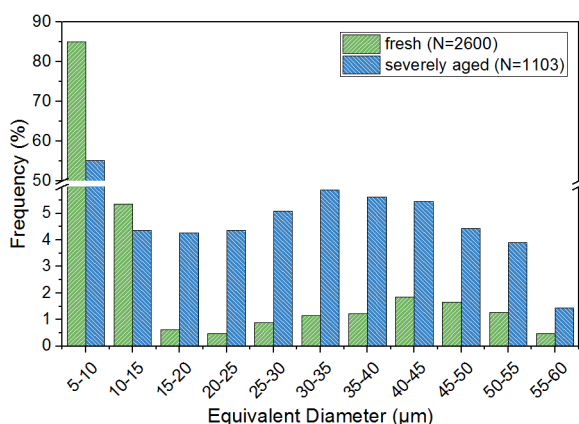

Figure 6. Comparison of the pore size distribution in the washcoat obtained from the high resolution μ-CT scans of the fresh and severely aged samples; N = number of analyzed pores.

Ptychographic X-ray Computed Tomography

As μ-CT was limited to observation of large macropores, synchrotron-based nanotomography was further applied to examine smaller macropores within the catalyst washcoat, including transport pores primarily used to promote gas diffusion. Notably even before the PXCT measurements, a strong

correlation between severity of the aging treatment and sample behavior during FIB preparation was observed. The aged and severely aged monolith washcoats were progressively more damaged and more prone to Ga$^+$ intrusion into the pore structure during FIB preparation than the freshly prepared monolith, as shown in Table 4. Since the FIB parameters for milling and manipulation were identical for each sample, this effect can only be attributed to changes in the washcoat structure. The presence of Ga was therefore used as a marker during PXCT for identification of unstable (Ga marked) and stable (Ga free) washcoat regions, as indicated in Figure 7. The reconstructed PXCT volume renderings clearly show the Ga marked exterior zones even for the fresh monolith (Figure 7c), which were segmented and removed before analyzing the sample porosity. The discarded segments were confirmed to contain high concentrations of Ga by complementary XRF mapping recorded simultaneously during PXCT (see supporting information Figure S8).

Table 4. Estimated sample size and Ga marked regions defined by PXCT measurements

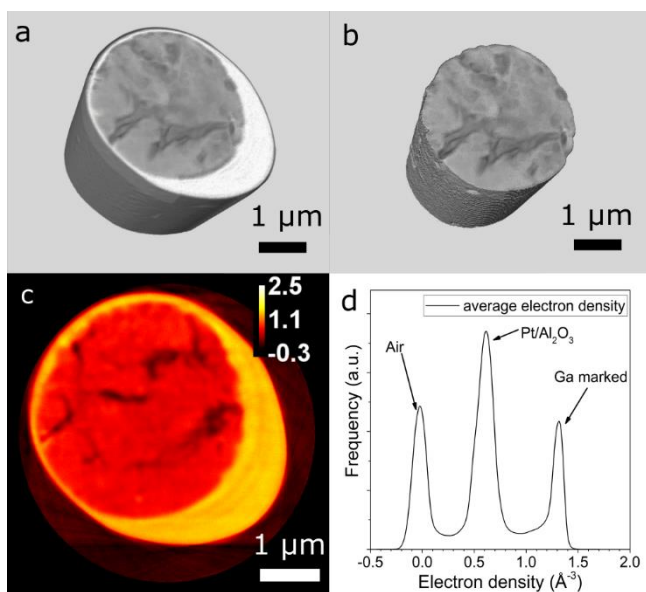| Monolith	Total sample volume [μm³]	Ga marked part [μm³]	Ga free part [μm³]	Ga marked part [%]
Fresh	59.3	16.7	42.6	28.2
Aged	80.6	28.1	52.5	34.9
Severely aged	24.0	11.4	12.6	47.5

Figure 7. Segmentation of reconstructed PXCT data for the fresh sample: (a) raw volume after filtering with visible Ga marked region; (b) after segmentation and removal of Ga marked region; (c) orthographic electron density map showing Ga marked zone, intact washcoat, and surrounding air in decreasing order of intensity; (d) electron density histogram of the volume shown in (a).

The reconstructed PXCT volumes for the fresh, aged and severely aged samples have spatial resolutions of around 35.3 nm, 47.8 nm and 41.0 nm, respectively. It was therefore possible to directly image the macropores (defined as >50 nm diameter) within the catalyst washcoat but not mesopores (defined as 2 to 50 nm diameter). The total porosity, estimated by voxel counting of segmented pores as a fraction of the total number of sample voxels in the segmented washcoat as displayed in Figure 7b, showed an increasing trend with aging (fresh: 4.6 %, aged: 21.6 %, severely aged: 33.4%). The size distribution of the macropores estimated by pore segmentation and label analysis is shown in Figure 8, and illustrates the collapse of the pore structure and the formation of large macropores up to 2 μm diameter due to aging. A graphical representation of the volumes used to create the histogram with highlighted pores, along with a typical orthographic slice illustrating the segmentation process can be found in the supplementary information (Figure S17-18). The median of the pore sizes shifts from 291.3

nm for the fresh, over 392.9 nm for the aged to over 465.1 nm for the severely aged sample. The results

match previous analysis by μ-CT (Figure 6), which also showed a significant shift towards formation of

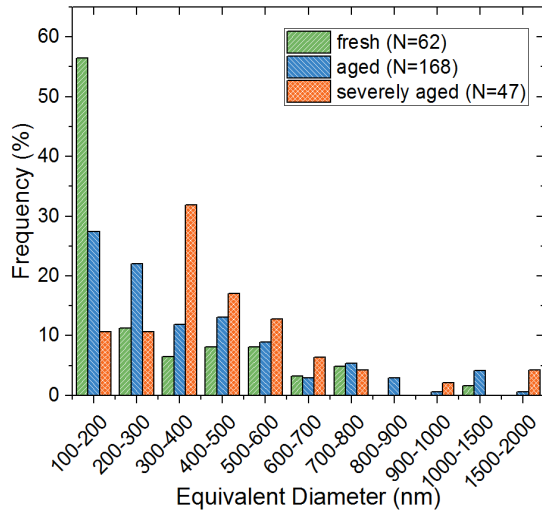large macropores in the 5 to 60 μm range following hydrothermal aging.

Figure 8. Relative pore size distribution of the fresh, aged and severely aged monolith washcoats

obtained from PXCT; N = number of analyzed pores.

Since PXCT is sensitive to local electron density of the probed area, the phase volumes acquired were

converted to electron density volumes for comparison of the solid washcoat structure [37]. The results

were compared to reference values calculated from the mass density of known sample constituents,

including pure Ga (1.58 Å^{-3}) and 4 wt.% Pt/Al$_2$O$_3$ with 10 wt.% SiO$_2$ (1.18 Å^{-3}), with the electron density of

surrounding air offset to zero. Note that these reference values indicate 'pure' material and do not

account for sample porosity. This approach can in principle provide an accurate estimation of electron

density given prior knowledge of the sample composition and mass density. In this way, deviations from

calculated reference values can potentially provide an indication of material porosity resulting from

partial volume effects (contribution of different materials to the measured intensity value of a voxel, in

this case micro-/mesopores and air) even where these cannot be directly visualized due to the resolution

limit. It should be noted that the visible macropores counted in Figure 8 were segmented as air (electron density = 0 Å^{-3}) and are not included in the following discussion of micro-/mesoporosity within the washcoat. The following electron density analysis is furthermore based on the following assumptions: (i) the average electron density histograms of each of the samples (Figure Figure **9**c,f,i) are representative of the bulk sample structure, (ii) no net change in elemental composition of the washcoat occurs due to (hydro)thermal aging, i.e. no material enters or leaves the washcoat due to disintegration, leaching or other mechanisms.

For each sample the measured electron density of three representative slices (for slice positions in volume see supporting information Figure S15) and the average electron density for the entire volumes are shown in Figure 9, providing a rich source of information on the sample composition. In the fresh sample, the washcoat showed an electron density peak at around 0.62 ±0.10 Å^{-3} (Figure 9b-c). Assuming a composition of 4 wt.% Pt, 10 wt.% SiO_2 and 86 wt.% Al_2O_3, this may correspond to combined micro- and mesoporosity of ca. 39 to 56%, compared to the reference value of 1.18 Å^{-3} for 4 wt.% Pt/ 10 wt.% SiO_2 /Al_2O_3. The Ga marked zones introduced by FIB preparation showed electron density of around 1.31 ±0.10 Å^{-3} (Figure 9a). This decrease from the reference value of 1.58 Å^{-3} for pure Ga supports the infusion of Ga of the porous structure of the Al_2O_3 washcoat. Assuming a median porosity of 50% in the outer washcoat, complete filling of the pores with pure Ga would result in a combined electron density of 1.38 Å^{-3}, which is in good agreement with the above analysis.
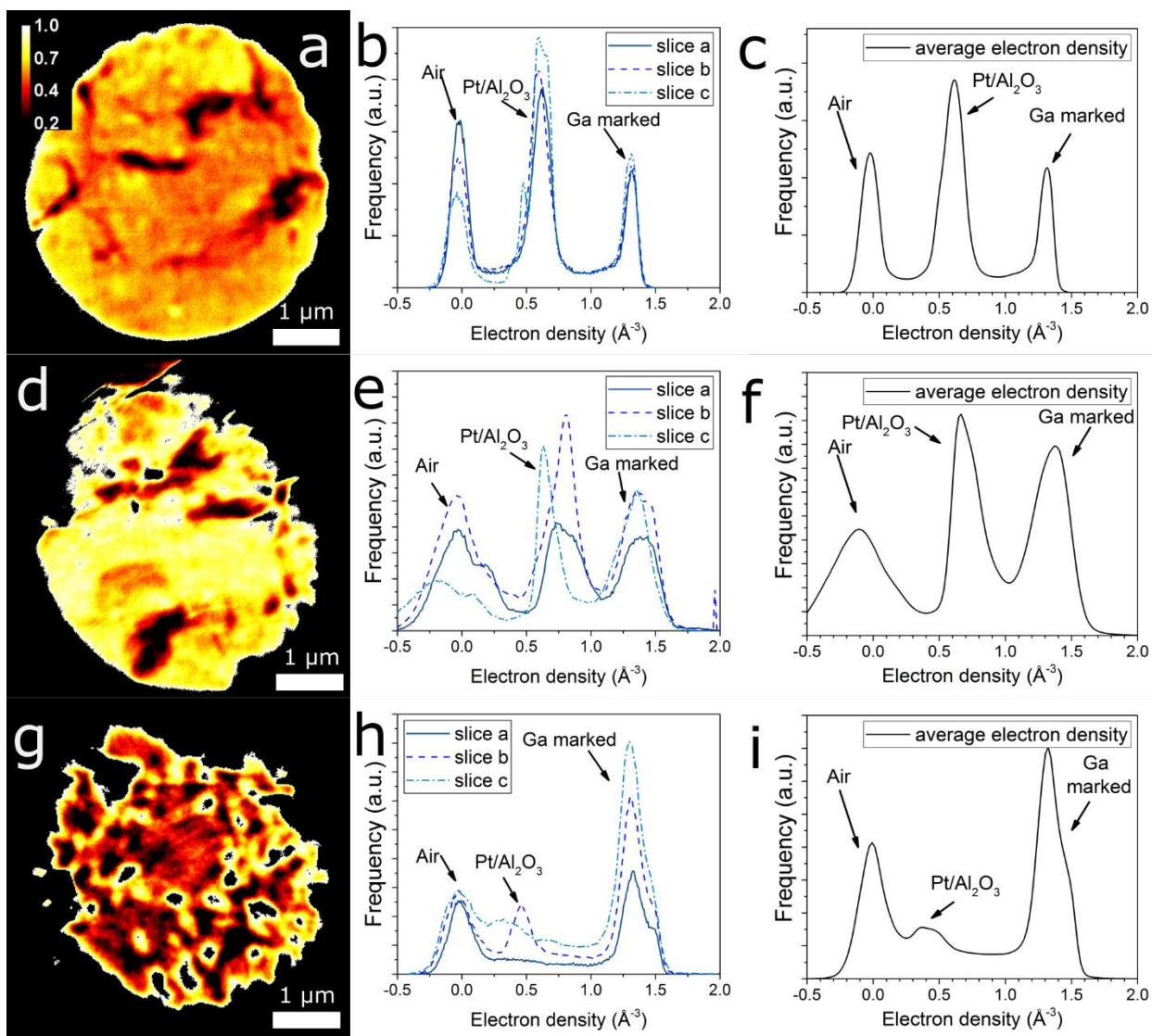
Figure 9. Representative electron density maps of a single slice (with Ga-marked region excluded) from:
(a) fresh; (d) aged; (g) severely aged monoliths, scale bars indicate electron density with air offset to
zero. Individual electron density histograms for: (b) fresh; (e) aged; (h) severely aged monoliths show
variation across three individual slices (see Figure S15). Average electron density histograms for: (c)
fresh; (f) aged; (i) severely aged monoliths show total values averaged for the entire PXCT volumes.

The aged sample showed a significant broadening of all three peaks and a shift of the Pt/Al_2O_3 peak to
higher electron densities (0.7-0.8 $Å^{-3}$) (Figure 9e-f) in comparison to the fresh sample. Peak broadening is
linked to the spatial resolution of the reconstructed volumes, which reflects the inferior spatial

resolution for the aged sample (ca. 48 nm) compared to the fresh (ca. 35 nm) or severely aged (ca. 41 nm) samples. The shift in maximum intensity of the Pt/Al_2O_3 peak may indicate an overall change in the composition (e.g. pores and solid Pt/Al_2O_3) of individual voxels. Assuming no material enters or leaves the washcoat and no change in elemental composition on thermal aging, this increased electron density can tentatively be assigned to a decrease in porosity, therefore densification of the sample. This is equivalent to a porosity decrease to ca. 37 to 51% compared to the reference values. The fact that the relative electron density increased rather uniformly across the volume (moving from Figure Figure **9**a,d), and the sample diameter of 5 μm likely excludes sintering of Pt as a possible cause of the electron density increase, which would be expected to occur rather locally. An additional feature with electron density of about 0.253 $Å^{-3}$ observed over several slices indicates the formation of large mesopores close to the resolution limit in the thermally treated sample (Figure 9e-f), consisting mainly of air. These were completely absent from the fresh sample (Figure Figure **9**c). The peak attributed to Ga infusion increased in relative intensity, indicating increased proportion of Ga in the sample and in good agreement with the larger Ga marked region observed for the aged sample compared to the fresh sample (Table 4). Furthermore, the change in symmetry in both the Pt/Al_2O_3 and Ga peaks which moved closer together, reflects the smaller contrast gradient observed between the Ga free and marked regions (Figure 9d) compared to the fresh sample (Figure 9a). This further supports the increased susceptibility of the washcoat to Ga infusion, as shown in Table Figure **4**. In summary, the results indicate conversion of micropores to larger mesopores and macropores within the washcoat as a result of thermal aging.

In the severely aged sample, the washcoat structure appeared highly fragmented (Figure 9g), resulting in significant reduction in intensity and increased broadening of the Pt/Al_2O_3 peak to around 0.3 to 0.6 $Å^{-3}$ (Figure 9h-i). The shift in the average Pt/Al_2O_3 peak maxima to lower values is in agreement with the fragmented structure, where a more extensive overlap of washcoat and air can be expected in comparison to the fresh and aged samples with largely intact washcoats. At the same time Ga showed a

23

greatly increased relative peak intensity, while the appearance of a shoulder at 1.50 $Å^{-3}$ on the primary

Ga peak indicates partial deposition of almost pure Ga and decomposition of the washcoat structure

(Figure 9h-i), in addition to Ga infusion into the washcoat observed previously. Several large Pt particles

with an electron density of > 4.0 $Å^{-3}$ (reference value for pure Pt: 5.17 $Å^{-3}$) also became visible over

several slices following hydrothermal aging (see Figure S8). This indicates extreme sintering of the active

metal nanoparticles to within the resolution limit of >41 nm in agreement with TEM analysis (Figure 3),

although here too few particles were visible to allow calculation of size distribution. It is sufficient to

note that sintering on a scale of 50 nm would severely decrease the active surface area, likely resulting in

the significant loss of activity observed previously (Figure 2) [17, 22].

Electron Tomography

To complement μ-CT and PXCT analysis of the global monolith structure, degradation of the washcoat

and the presence of macropores, ET was applied to further resolve the finer micro- and mesopore

structure of the monoliths. While the sample size in electron microscopy is strictly limited, the resolution

obtained far exceeds that of any X-ray microscopy method, in this case approximately 1.2 nm was

obtained for the reconstructed ET volumes shown in Figure 10, left. The achieved contrast between pore

volume and washcoat material is sufficient to distinguish them as shown in Figure 10. As the samples

were removed by physical abrasion from the monoliths, there is significant variation in the studied

sample volume, with the aged sample (2.7×10^7 nm³) approximately 3.5 times bigger than the fresh

sample (9.6×10^6 nm³). Note that the pores studied by ET are primarily mesopores and some big

micropores, which are significantly below the resolution limit for PXCT, this is equivalent to the porosity

estimated within the washcoat based on electron density shown previously (Figure 9). In the fresh

sample the pores take up a volume of 45.2 % of the measured grain, while in the aged sample the total

pore-volume decreased to 29.9 %. This is consistent with the increased electron density observed in the

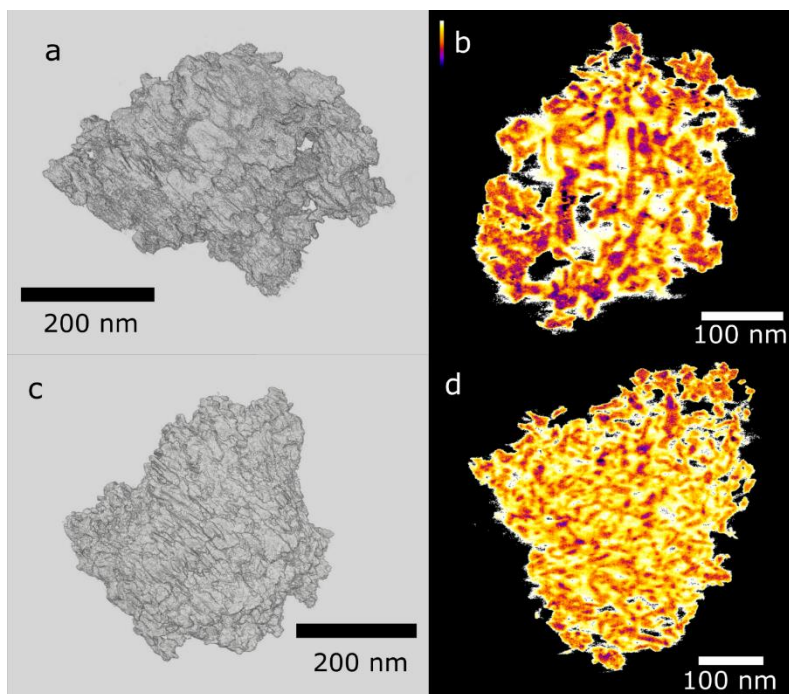catalyst washcoat by PXCT, which indicated approximately 47.5 % porosity in the fresh and 44.1 % in the aged samples.

Figure 10. Reconstructed volumes of the fresh (a) and aged (c) monoliths obtained by ET with ca. 1.5 nm resolution. Orthographic slice through the reconstruction of the fresh (b) and aged (d) monolith, showing visible contrast difference between washcoat material (bright orange) and pore volume (dark orange)

The pore size distribution for the fresh and aged samples is shown in Figure 11a. The fresh monolith showed mainly mesopores with the most frequent pore diameters in the range of 25 to 40 nm. In contrast, the aged sample showed a distinctive shift towards both smaller pores in the range of 5 to 15 nm, and larger mesopores of >45 nm. In contrast to the increasing macropore distribution obtained by PXCT after aging, it is notable that the relative number of micro- and mesopores counted by ET decreased by around 40% with thermal aging of the sample, when normalized to the sample volume. It should also be noted that here no specific distinction was made between open and enclosed pores, the latter of which do not contribute the accessible pore structure [42], although such analysis is feasible with

the tomography data acquired. Following hydrothermal treatment, the pore structure of the severely

aged catalyst appeared to be significantly damaged, with few visible meso- or micropores and large

agglomerations of the alumina support material observed, therefore no tomogram was recorded and no

porosity analysis performed. The tomograms also allowed visualization and counting of Pt particles

within the washcoat which were segmented and labelled based on contrast in the same manner as the

pores. The Pt size distribution observed for the fresh and aged sample is shown in Figure 11b. For the

fresh catalyst, over 70% of Pt particles were within the 1 to 3 nm size range, while an average particle

size of 8 nm was observed for the aged monolith, including over 40% of particles of 10 to 20 nm

diameter and a further 30% in the 3 to 6 nm range. The size distribution of the Pt particles obtained from

STEM tomography generally matches the results of STEM characterization shown previously (Figure 3).
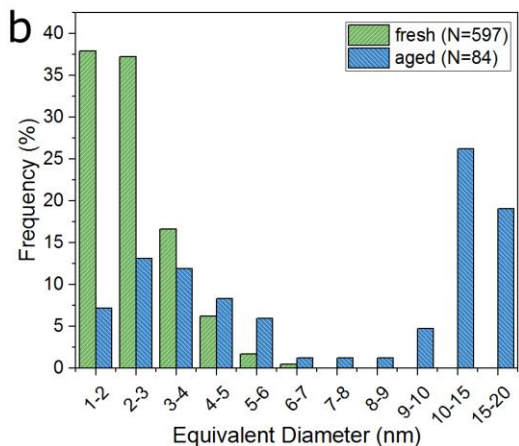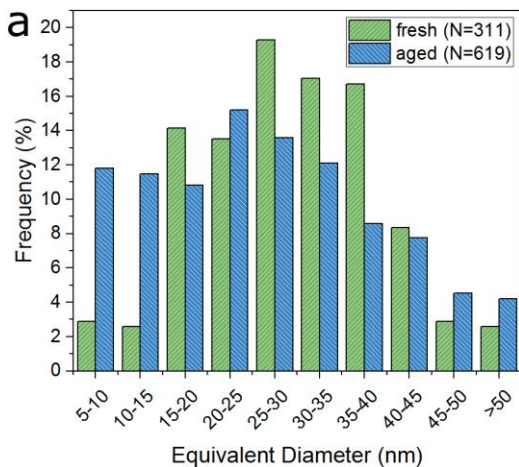
Figure 11. Washcoat characteristics from analysis of the reconstructed ET volumes: (a) pore size distribution of the fresh and aged sample, N = number of counted pores; (b) Pt particle size distribution in the fresh and aged sample, N = number of counted particles.

Influence of (hydro)thermal aging on the catalyst structure

Two main effects were investigated in this work, sintering of Pt metal in the washcoat, and changes in porosity and structural integrity of the washcoat from nm to cm scale. In both cases, the advantages of a highly spatially-resolved analytical approach are demonstrated. Initial catalytic tests showed decreased CO oxidation performance, indicating the occurrence of progressive catalyst deactivation. Thermal and hydrothermal aging were expected to induce increasingly severe sintering of the Pt particles, which was observed by all analytical methods applied [44, 57]. Thermal treatment resulted in formation of Pt particles up to approximately 10 nm diameter, while hydrothermal treatment caused extreme sintering. Quantification of particle size distribution was provided by TEM and ET, while for the hydrothermally aged sample Pt sintering was so severe as to be visible with PXCT. At the same time, sintering processes were likely coupled to or enabled by notable changes in the catalyst washcoat structure, in terms of porosity and also global stability. BET and BJH analysis showed significant decrease in surface area and increase in average pore diameter after aging, indicative of a transition from micropores to larger mesopores and macropores. These effects were thoroughly investigated with multiscale tomographic imaging, offering deep insight into the behavior of micro- meso- and macroporosity within the washcoat following the aging conditions applied.

In general, thermal aging was found to decrease the micropore and mesopore volume of the catalyst washcoat, while at the same time increasing the formation of larger macropores from several hundred nm up to 60 μm diameter, confirming the results of N_2-physisorption on the bulk catalyst. This was observed both by physical counting of smaller pores from ET and macropores by PXCT, supported by quantitative electron density calculations on the observed washcoat. Such results at the spatial

resolutions obtained here are only feasible using the unique combination of ET and PXCT, covering the

nm to µm scale. To complement this and account for the limited sample volumes permitted with higher

resolution techniques, laboratory µ-CT was used to visualize the macroscopic properties of the catalyst.

This supported the observation of large macropore formation, together with cracking and damage to the

catalyst washcoat following hydrothermal treatment. It should be noted that the total pore volume

observed by each tomography technique differed significantly, although this is related to differences in

spatial resolution and sample size. In any case, the visible porosity has a different meaning depending on

the measurement, for example the decrease in mesoporosity observed by ET clearly leads to a decrease

in accessible catalyst surface area, while conversely an increase in macroporosity observed by PXCT and

µ-CT also leads to a decrease in surface area. Hence, the expansion or connection of nearby mesopores

to form macropores should lead to a cumulative reduction in surface area. The same general trend of

decreased effective surface area and increased presence of macropores was therefore repeatedly

observed by each tomography technique. In summary, the balance between high resolution techniques

on small sample volumes which may not be representative of the bulk material must be carefully

considered against lower resolution techniques on larger sample volumes [58]. For example, the pore sizes

measured by PXCT for the treated samples are the same order of magnitude of the entire sample volume

examined by means of ET. This shows the relevance of combining different length scales to gain a more

complete understanding of porosity, and the need to employ spatially-resolved characterization instead

of one-dimensional bulk analysis.

Future studies may focus on the measurement of identical sample volumes following sequential

(hydro)thermal treatment for a more accurate interpretation of porosity changes. This was previously

demonstrated for synchrotron-based microtomography [44], but is potentially feasible also for

nanotomography. The ideal case study would be an in situ measurement under different aging

conditions [59]. However, this requires a sophisticated experimental setup and in the case of hydrothermal

aging, the application of relatively harsh reaction conditions. In addition, further studies may aim to investigate larger sample volumes, and to selectively extract samples from different depths and positions (e.g. edge or corner) around the washcoat. This would provide a more accurate determination of the distribution of pores in 3D space, for the purposes of modeling and simulation. Accurate determination of pore size distribution, including colocation in 3D space unique to tomography, may provide an input for future modelling studies and computational analysis of gas diffusion, mass and heat transport [12]. This could constitute a valuable alternative to porosity simulations. Finally, the imminent arrival of 4th generation diffraction-limited synchrotron light sources is expected to dramatically improve the quality and spatial resolution of coherent X-ray microscopy measurements such as PXCT. Improved spatial resolution will offer greater sensitivity to small structural changes, in contrast to the extreme aging conditions applied in this study, and may therefore broaden the experimental application to include gradual sample aging under realistic catalyst treatment conditions. This will potentially allow larger more representative sample volumes to be measured in a short time, and further establish PXCT as an optimal technique to address the 'resolution gap' which currently persists between synchrotron micro-/nanotomography techniques and electron microscopy. This will offer powerful new potential for deep characterization of catalysts and porous materials, with an aim to understand structure-activity relationships and deactivation processes.

Conclusion

Spatially-resolved characterization of exhaust gas monolith catalysts over length scales from nm to cm was performed using complementary electron and X-ray tomographic imaging. The effects of thermal and hydrothermal aging on the catalyst washcoat were examined, particularly with respect to sintering of Pt metal and changes in washcoat porosity. Aging treatments resulted in decreased micro and mesoporosity, and increased formation of macropores within the catalyst washcoat. These changes were

individually determined and corroborated by tomographic analysis on multiple length scales. Hard X-ray microscopy using synchrotron radiation and particularly PXCT has proven to be a promising method, combining high resolution imaging with extended sample volumes, and chemical contrast by means of electron density calculations. PXCT effectively fills the resolution gap between electron microscopy and microtomography, and its impact is expected to increase with the development of diffraction-limited synchrotron light sources. The obtained 3D volume data may provide valuable input for simulation and modelling studies, replacing the use of calculated volumes with real volumetric data on the size and location of porous features. A deeper understanding of aging processes and resulting improvements in modelling and simulation may promote knowledge-driven design of future catalysts. Modern characterization of catalyst deactivation processes should ideally consider spatially-resolved analysis such as tomography which reveals a high degree of material complexity, in order to link changes in activity to real changes in the complex hierarchical structure of the catalyst.

Acknowledgements

Supporting Information

N2-physisorption, BET and BJH plots; Pt particle size distribution analysis; CO oxidation tests and light-

off curves; FIB preparation for PXCT; complementary XRF tomography and XRD signals; additional µ-CT

images; additional image reconstruction and processing details; PXCT histograms, pore analysis and

electron density calculations; ET histograms, pore analysis and sharp edge fitting; FSC spatial resolution

estimates for PXCT. Tomographic data files and 3D renderings of the data shown in this work may be

provided directly upon reasonable request.

References

1.   Deutschmann, O.; Grunwaldt, J.-D., Exhaust Gas Aftertreatment in Mobile Systems: Status, Challenges, and Perspectives. *Chem. Ing. Tech.* **2013**, *85*, 595-617.
2.   Votsmeier, M.; Kreuzer, T.; Gieshoff, J.; Lepperhoff, G., Automobile Exhaust Control. In *Ullmann's Encyclopedia of Industrial Chemistry*, Wiley-VCH Verlag GmbH & Co. KGaA.: Weinheim, Germany, 2000.
3.   Twigg, M. V., Catalytic Control of Emissions from Cars. *Catal. Today* **2011**, *163*, 33-41.
4.   Lox, E. S., Automotive Exhaust Treatment. In *Handbook of Heterogeneous Catalysis: Online*, Ertl, G.; Knözinger, H.; Schüth, F.; Weitkamp, J., Eds. Wiley-VCH Verlag GmbH & Co. KGaA.: Weinheim, Germany, 2008; pp 2274-2345.
5.   Gremminger, A. T.; de Carvalho, H. W. P.; Popescu, R.; Grunwaldt, J.-D.; Deutschmann, O., Influence of Gas Composition on Activity and Durability of Bimetallic Pd-Pt/Al2O3 Catalysts for Total Oxidation of Methane. *Catal. Today* **2015**, *258*, 470-480.
6.   Russell, A.; Epling, W. S., Diesel Oxidation Catalysts. *Catal. Rev.* **2011**, *53*, 337-423.

7.   Hazlett, M. J.; Epling, W. S., Heterogeneous Catalyst Design: Zoned and Layered Catalysts in Diesel Vehicle Aftertreatment Monolith Reactors. *Can. J. Chem. Eng.* **2019**, *97*, 188-206.

8.   Doronkin, D. E.; Lichtenberg, H.; Grunwaldt, J.-D., Cell Designs for in Situ and Operando Studies. In *Xafs Techniques for Catalysts, Nanomaterials, and Surfaces*, Iwasawa, Y.; Asakura, K.; Tada, M., Eds. Springer International Publishing: Cham, 2017; pp 75-89.

9.   Ivanova, A. S.; Slavinskaya, E. M.; Gulyaev, R. V.; Zaikovskii, V. I.; Stonkus, O. A.; Danilova, I. G.; Plyasova, L. M.; Polukhina, I. A.; Boronin, A. I., Metal–Support Interactions in Pt/Al2O3 and Pd/Al2O3 Catalysts for CO Oxidation. *Appl. Catal. B.* **2010**, *97*, 57-71.

10.   Singh, J.; Alayon, E. M. C.; Tromp, M.; Safonova, O. V.; Glatzel, P.; Nachtegaal, M.; Frahm, R.; van Bokhoven, J. A., Generating Highly Active Partially Oxidized Platinum During Oxidation of Carbon Monoxide over Pt/Al2O3: In Situ, Time-Resolved, and High-Energy-Resolution X-Ray Absorption Spectroscopy. *Angew. Chem.* **2008**, *120*, 9400-9404.

11.   Martin, N. M., Nilsson, J., Skoglundh, M., Adams, E.C., Wang, X., Velin, P., Smedler, G., Raj, A., Thompsett, D., Brongersma, H.H., et al., Characterization of Surface Structure and Oxidation/Reduction Behavior of Pd–Pt/Al2O3 Model Catalysts. *J. Phys. Chem. C* **2016**, *120*, 28009-28020.

12.   Caravella, A.; Hara, S.; Hara, N.; Obuchi, A.; Uchisawa, J., Three-Dimensional Modeling and Simulation of a Micrometer-Sized Particle Hierarchical Structure with Macro- and Meso-Pores. *Chem. Eng. J.* **2012**, *210*, 363-373.

13.   Santos, H.; Pires, J.; Costa, M., Influence of the Washcoat Structure in the Performance of Automotive Three Way Catalysts. SAE International: 2013; Vol. 6, pp 1846-1854.

14.   Uchisawa, J.; Obuchi, A.; Nanba, T.; Hara, S.; Caravella, A.; Tango, T.; Murakami, T.; Nakagawa, H.; Kogawa, T.; Abe, A., Effect of Macropore Formation in Pt Catalyst Supports on the Oxidation Activity for Diesel Fuel Mist. *Ind. Eng. Chem. Res.* **2012**, *51*, 719-724.

15.   More, H.; Hayes, R. E.; Liu, B.; Votsmeier, M.; Checkel, M. D., The Effect of Catalytic Washcoat Geometry on Light-Off in Monolith Reactors. *Top. Catal.* **2006**, *37*, 155-159.

16.   Cordiner, S.; De Simone, G.; Mulone, V., Influence of Washcoat Distribution on the Performance of Diesel Oxidation Catalysts. SAE International: 2007; Vol. 2007-01-4007.

17.   Chan, D.; Tischer, S.; Heck, J.; Diehm, C.; Deutschmann, O., Correlation between Catalytic Activity and Catalytic Surface Area of a Pt/Al2O3 DOC: An Experimental and Microkinetic Modeling Study. *Appl. Catal. B.* **2014**, *156-157*, 153-165.

18.   Stoeckel, D.; Kübel, C.; Hormann, K.; Höltzel, A.; Smarsly, B. M.; Tallarek, U., Morphological Analysis of Disordered Macroporous–Mesoporous Solids Based on Physical Reconstruction by Nanoscale Tomography. *Langmuir* **2014**, *30*, 9022-9027.

19.   Weckhuysen, B. M., Chemical Imaging of Spatial Heterogeneities in Catalytic Solids at Different Length and Time Scales. *Angew. Chem. Int. Ed.* **2009**, *48*, 4910-4943.

20.   Müllner, T.; Zankel, A.; Lv, Y.; Svec, F.; Höltzel, A.; Tallarek, U., Assessing Structural Correlations and Heterogeneity Length Scales in Functional Porous Polymers from Physical Reconstructions. *Adv. Mater.* **2015**, *27*, 6009-6013.

21.   Mitchell, S.; Michels, N.-L.; Majano, G.; Pérez-Ramírez, J., Advanced Visualization Strategies Bridge the Multidimensional Complexity of Technical Catalysts. *Curr. Op. Chem. Eng.* **2013**, *2*, 304-311.

22.   Winkler, A.; Ferri, D.; Aguirre, M., The Influence of Chemical and Thermal Aging on the Catalytic Activity of a Monolithic Diesel Oxidation Catalyst. *Appl. Catal. B.* **2009**, *93*, 177-184.

23.   Tariq, F.; Lee, P. D.; Haswell, R.; McComb, D. W., The Influence of Nanoscale Microstructural Variations on the Pellet Scale Flow Properties of Hierarchical Porous Catalytic Structures Using Multiscale 3d Imaging. *Chem. Eng. Sci.* **2011**, *66*, 5804-5812.

24.   Grunwaldt, J.-D.; Schroer, C. G., Hard and Soft X-Ray Microscopy and Tomography in Catalysis: Bridging the Different Time and Length Scales. *Chem. Soc. Rev.* **2010**, *39*, 4741-4753.

25.   Meirer, F.; Weckhuysen, B. M., Spatial and Temporal Exploration of Heterogeneous Catalysts with Synchrotron Radiation. *Nat. Rev. Mater.* **2018**, *3*, 324-340.

26.   Mitchell, S.; Michels, N.-L.; Majano, G.; Pérez-Ramírez, J., Advanced Visualization Strategies Bridge the Multidimensional Complexity of Technical Catalysts. *Curr. Opin. Chem. Eng.* **2013**, *2*, 304.

27.   Karakaya, C.; Weddle, P. J.; Blasi, J. M.; Diercks, D. R.; Kee, R. J., Modeling Reaction–Diffusion Processes within Catalyst Washcoats: I. Microscale Processes Based on Three-Dimensional Reconstructions. *Chem. Eng. Sci.* **2016**, *145*, 299-307.

28.   Kočí, P.; Isoz, M.; Plachá, M.; Arvajová, A.; Václavík, M.; Svoboda, M.; Price, E.; Novák, V.; Thompsett, D., 3d Reconstruction and Pore-Scale Modeling of Coated Catalytic Filters for Automotive Exhaust Gas Aftertreatment. *Catal. Today* **2019**, *320*, 165-174.

29.   Dong, Y.; Korup, O.; Gerdts, J.; Roldán Cuenya, B.; Horn, R., Microtomography-Based Cfd Modeling of a Fixed-Bed Reactor with an Open-Cell Foam Monolith and Experimental Verification by Reactor Profile Measurements. *Chem. Eng. J.* **2018**, *353*, 176-188.

30.   Koster, A. J.; Ziese, U.; Verkleij, A. J.; Janssen, A. H.; de Jong, K. P., Three-Dimensional Transmission Electron Microscopy: A Novel Imaging and Characterization Technique with Nanometer Scale Resolution for Materials Science. *J. Phys. Chem. B* **2000**, *104*, 9368-9370.

31.   Rösner, H.; Parida, S.; Kramer, D.; Volkert, C. A.; Weissmüller, J., Reconstructing a Nanoporous Metal in Three Dimensions: An Electron Tomography Study of Dealloyed Gold Leaf. *Adv. Eng. Mater.* **2007**, *9*, 535-541.

32.   Fujita, T.; Qian, L.-H.; Inoke, K.; Erlebacher, J.; Chen, M.-W., Three-Dimensional Morphology of Nanoporous Gold. *Appl. Phys. Lett.* **2008**, *92*, 251902.

33.   Friedrich, H.; de Jongh, P. E.; Verkleij, A. J.; de Jong, K. P., Electron Tomography for Heterogeneous Catalysts and Related Nanostructured Materials. *Chem. Rev.* **2009**, *109*, 1613-1629.

34.   Pfeiffer, F., X-Ray Ptychography. *Nat. Photonics* **2018**, *12*, 9-17.

35.   Dierolf, M.; Menzel, A.; Thibault, P.; Schneider, P.; Kewish, C. M.; Wepf, R.; Bunk, O.; Pfeiffer, F., Ptychographic X-Ray Computed Tomography at the Nanoscale. *Nature* **2010**, *467*, 436-439.

36.   Thibault, P.; Dierolf, M.; Menzel, A.; Bunk, O.; David, C.; Pfeiffer, F., High-Resolution Scanning X-Ray Diffraction Microscopy. *Science* **2008**, *321*, 379-382.

37.   Diaz, A.; Trtik, P.; Guizar-Sicairos, M.; Menzel, A.; Thibault, P.; Bunk, O., Quantitative X-Ray Phase Nanotomography. *Phys. Rev. B* **2012**, *85*, 020104.

38.   Ihli, J., Jacob, R.R., Holler, M., Guizar-Sicairos, M., Diaz, A., da Silva, J.C., Ferreira Sanchez, D., Krumeich, F., Grolimund, D., Taddei, M., et al., A Three-Dimensional View of Structural Changes Caused by Deactivation of Fluid Catalytic Cracking Catalysts. *Nat. Commun.* **2017**, *8*, 809.

39.   Holler, M.; Diaz, A.; Guizar-Sicairos, M.; Karvinen, P.; Färm, E.; Härkönen, E.; Ritala, M.; Menzel, A.; Raabe, J.; Bunk, O., X-Ray Ptychographic Computed Tomography at 16 nm Isotropic 3d Resolution. *Sci. Rep* **2014**, *4*, 10.1038.

40.   Reinhardt, J., Hoppe, R., Hofmann, G., Damsgaard, C.D., Patommel, J., Baumbach, C., Baier, S., Rochet, A., Grunwaldt, J.-D., Falkenberg, G., et al., Beamstop-Based Low-Background Ptychography to Image Weakly Scattering Objects. *Ultramicroscopy* **2017**, *173*, 52-57.

41.   Wise, A. M.; Weker, J. N.; Kalirai, S.; Farmand, M.; Shapiro, D. A.; Meirer, F.; Weckhuysen, B. M., Nanoscale Chemical Imaging of an Individual Catalyst Particle with Soft X-Ray Ptychography. *ACS Catal.* **2016**, *6*, 2178-2181.

42.   da Silva, J. C., Mader, K., Holler, M., Haberthür, D., Diaz, A., Guizar-Sicairos, M., Cheng, W.-C., Shu, Y., Raabe, J., Menzel, A., et al., Assessment of the 3 D Pore Structure and Individual Components of Preshaped Catalyst Bodies by X-Ray Imaging. *ChemCatChem* **2015**, *7*, 413-416.

43.   Baier, S., Damsgaard, C.D., Scholz, M., Benzi, F., Rochet, A., Hoppe, R., Scherer, T., Shi, J., Wittstock, A., Weinhausen, B., et al., In Situ Ptychography of Heterogeneous Catalysts Using Hard X-Rays: High Resolution Imaging at Ambient Pressure and Elevated Temperature. *Microsc. Microanal.* **2016**, *22*, 178-188.

44.   Hofmann, G.; Rochet, A.; Ogel, E.; Casapu, M.; Ritter, S.; Ogurreck, M.; Grunwaldt, J.-D., Aging of a Pt/Al2o3 Exhaust Gas Catalyst Monitored by Quasi in Situ X-Ray Micro Computed Tomography. *RSC Adv.* **2015**, *5*, 6893-6905.

45.   Feldkamp, L. A.; Davis, L. C.; Kress, J. W., Practical Cone-Beam Algorithm. *J. Opt. Soc. Am. A* **1984**, *1*, 612-619.

46.   Stierle, A.; Keller, T. F.; Noei, H.; Vonk, V.; Roehlsberger, R., Desy Nanolab. *Journal of large-scale research facilities* **2016**, *2*.

47.   Maiden, A. M.; Rodenburg, J. M., An Improved Ptychographical Phase Retrieval Algorithm for Diffractive Imaging. *Ultramicroscopy* **2009**, *109*, 1256-1262.

48.   Guizar-Sicairos, M.; Diaz, A.; Holler, M.; Lucas, M. S.; Menzel, A.; Wepf, R. A.; Bunk, O., Phase Tomography from X-Ray Coherent Diffractive Imaging Projections. *Opt. Express* **2011**, *19*, 21345-21357.

49.   Dowd, B. A.; Campbell, G. H.; Marr, R. B.; Nagarkar, V. V.; Tipnis, S. V.; Axe, L.; Siddons, D. P. In *Developments in Synchrotron X-Ray Computed Microtomography at the National Synchrotron Light Source*, Developments in X-ray Tomography II, International Society for Optics and Photonics: 1999; pp 224-237.

50.   Gürsoy, D.; De Carlo, F.; Xiao, X.; Jacobsen, C., Tomopy: A Framework for the Analysis of Synchrotron Tomographic Data. *J. Synchrotron Radiat.* **2014**, *21*, 1188-1193.

51.   van Heel, M.; Schatz, M., Fourier Shell Correlation Threshold Criteria. *J. Struct. Biol.* **2005**, *151*, 250-262.

52.   Crowther, R. A.; DeRosier, D.; Klug, A., The Reconstruction of a Three-Dimensional Structure from Projections and Its Application to Electron Microscopy. *Proc. R. Soc. Lond. A* **1970**, *317*, 319-340.

53.   Casapu, M.; Fischer, A.; Gänzler, A. M.; Popescu, R.; Crone, M.; Gerthsen, D.; Türk, M.; Grunwaldt, J.-D., Origin of the Normal and Inverse Hysteresis Behavior During Co Oxidation over Pt/Al2O3. *ACS Catal.* **2017**, *7*, 343-355.

54.   Ogel, E.; Casapu, M.; Doronkin, D. E.; Popescu, R.; Störmer, H.; Mechler, C.; Marzun, G.; Barcikowski, S.; Türk, M.; Grunwaldt, J. D., Impact of Preparation Method and Hydrothermal Aging on Particle Size Distribution of Pt/Γ-Al2o3 and Its Performance in Co and No Oxidation. *J. Phys. Chem. C* **2019**, *123*, 5433-5446.

55.   Dhillon, P. S.; Harold, M. P.; Wang, D.; Kumar, A.; Joshi, S., Hydrothermal Aging of Pt/Al2O3 Monolith: Washcoat Morphology Degradation Effects Studied Using Ammonia and Propylene Oxidation. *Catal. Today* **2019**, *320*, 20-29.

56.   Löwendahl, L.; Otterstedt, J. E., Effect of Hydrothermal Treatment on Alumina as Support for Noble Metal Catalysts. *Appl. Catal.* **1990**, *59*, 89-102.

57.   Andersson, J.; Antonsson, M.; Eurenius, L.; Olsson, E.; Skoglundh, M., Deactivation of Diesel Oxidation Catalysts: Vehicle- and Synthetic Aging Correlations. *Appl. Catal. B.* **2007**, *72*, 71-81.

58.   Larsson, E.; Gursoy, D.; De Carlo, F.; Lilleodden, E.; Storm, M.; Wilde, F.; Hu, K.; Muller, M.; Greving, I., Nanoporous Gold: A Hierarchical and Multiscale 3d Test Pattern for Characterizing X-Ray Nano-Tomography Systems. *J. Synchrotron Radiat.* **2019**, *26*, 194-204.

59.   Vamvakeros, A., Jacques, S.D.M., Di Michiel, M., Matras, D., Middelkoop, V., Ismagilov, I.Z., Matus, E.V., Kuznetsov, V.V., Drnec, J., Senecal, P., et al., 5D Operando tomographic Diffraction Imaging of a Catalyst Bed. *Nat. Commun.* **2018**, *9*, 4751.

TOC Graphic